The Cryosphere Discuss., 8, 3117–3139, 2014
www.the-cryosphere-discuss.net/8/3117/2014/
doi:10.5194/tcd-8-3117-2014

The Cryosphere Discussions
Open Access

Quantifying mass balance processes on the Southern Patagonia Icefield

M. Schaefer[1,2], H. Machguth[3], M. Falvey[4], G. Casassa[5,6], and E. Rignot[7,8]

[1]Instituto de Ciencias Físicas y Matematicas, Facultad de Ciencias, Universidad Austral de Chile, Valdivia, Chile
[2]Instituto de Ciencias Marinas y Limnológicas, Facultad de Ciencias, Universidad Austral de Chile Valdivia, Chile
[3]Arctic Technology Centre, Technical University of Denmark, Kgs. Lyngby, Denmark
[4]Department of Geophysics, Universidad de Chile, Santiago, Chile
[5]Geoestudios, Las Vertientes, San José de Maipo, Chile
[6]Universidad de Magallanes, Punta Arenas, Chile
[7]Jet Propulsion Laboratory, Pasadena, USA
[8]University of California, Department of Earth System Science, Irvine, USA

Received: 9 April 2014 – Accepted: 16 May 2014 – Published: 11 June 2014

Correspondence to: M. Schaefer (mschaefer@uach.cl)

Published by Copernicus Publications on behalf of the European Geosciences Union.

Abstract

We present surface mass balance simulations of the Southern Patagonia Icefield driven by downscaled reanalysis data. The simulations were validated and interpreted using geodetic mass balances, measured point balances and a complete velocity field of the Icefield from spring 2004. The high measured accumulation of snow as well as the high measured ablation is reproduced by the model. The overall modeled surface mass balance was positive and increasing during 1975–2011. Subtracting the surface mass balance from geodetic balances, calving fluxes were inferred. Mass losses of the SPI due to calving were strongly increasing from 1975–2000 to 2000–2011 and higher than losses due to surface melt. Calving fluxes were inferred for the individual glacier catchments and compared to fluxes estimated from velocity data. Measurements of ice thickness and flow velocities at the glaciers' front and spatially distributed accumulation measurements can help to reduce the uncertainties of the different terms in the mass balance of the Southern Patagonia Icefield.

1 Introduction

The Southern Patagonia Icefield (SPI, Fig. 1) is the largest ice mass in the Southern Hemisphere outside of Antarctica. The great majority of its outlet glaciers have been retreating and thinning at high rates in recent decades (Rignot et al., 2003; Masiokas et al., 2009; López et al., 2010; Willis et al., 2012b). Mass balance processes for most of the glaciers of the SPI, however, are poorly quantified, which makes it difficult to understand the reasons for the fast ice loss from the SPI. Increase in surface melt, decrease in accumulation or changes in the ice dynamics are possible candidates. Another explanation could be sub-glacial volcanic activity (Orihashi et al., 2004) which is motivated by the fact that the SPI coincides with four volcanoes of the Andean Austral Volcanic Zone (Stern, 2004, 2008).

Locally varying warming trends have been observed in Southern South America in the last century with rates up to 0.028 °C year^{-1} next to the Atlantic Ocean (Rosenblüth et al., 1995; Ibarzabal y Donangelo et al., 1996; Rasmussen et al., 2007; Falvey and Garreaud, 2009). Large inter-annual and inter-decadal variations of precipitation have been observed in Patagonia, although with no significant overall trends in the last century (Rosenblüth et al., 1995; Carrasco et al., 2002; Aravena and Luckman, 2009).

Prominent acceleration of the ice flow (and therefore ice loses due to calving) were detected at the Glaciers Jorge Montt (Rivera et al., 2012a) and Upsala (Jaber et al., 2012; Sakakibara et al., 2013). For both glaciers a fast retreat of the glacier was observed together with the acceleration.

The surface mass balance was modeled for two glaciers of the SPI: Chico Glacier (Rivera, 2004) and Perito Moreno Glacier (Stuefer et al., 2007), both using degree-day-models. In 1975–2001 Rivera (2004) obtained an average negative yearly surface mass balance of Chico Glacier, which was showing high inter-annual variations and a slightly negative trend. Stuefer et al. (2007) obtained a near to zero cumulative glacier mass balance for the Perito Moreno Glacier between 1973 and 2000, with the annual specific balances varying between +1 mweq and −1 mweq.

A combined modeling approach was recently applied on the Northern Patagonia Icefield (NPI) (Schaefer et al., 2013): global meteorological data were downscaled using the regional climate model Weather Research and Forecasting and statistical downscaling techniques. These data were used to drive a surface mass balance model of intermediate complexity (Oerlemans, 2001). An increase of accumulation was detected over the NPI during 1975–2011. The increased observed mass loss of the NPI in 2000–2011 (Willis et al., 2012a) as compared to 1975–2000 (Rignot et al., 2003) was explained by an increase of losses by calving.

In this contribution a similar methodology is applied to make first inferences of the components of the mass balance of the SPI as a whole and for its individual glacier catchments. We give a summary of the methods applied in Sect. 2. In Sect. 3 we present the results, discuss them and in Sect. 4 we draw the conclusions of our study.

2 Methods

To obtain realistic meteorological input data for the surface mass balance model in the modeling period 1975–2011, a downscaling procedure has been realized, which includes various steps (Schaefer et al., 2013). In a first step, version 3.2 of the Advanced Research Weather Research and Forecasting model (WRF-model hereafter) was run for a 7 year period from 2005 until 2011, using a nested computational grid (five point relaxation zone between grids), with the inner grid having a spatial resolution of 5 km over an area of 675 km × 425 km that includes both the NPI and SPI. The model was forced at its boundaries by NCEP-NCAR atmospheric reanalysis data (Kalnay et al., 1996), which consist of three-dimensional atmospheric fields on a 2.5° resolution grid at 6 h intervals. The WRF-model's output was saved at hourly intervals, which were used to yield the daily averages required by the mass balance model. To obtain downscaled meteorological data for the entire 1975–2011-period, statistical downscaling techniques were applied similar to the ones used to relate local climate observations to large scale atmospheric parameters that are predicted by low resolution Global Circulation Models (Fowler et al., 2007). The basic assumption is that local variability (which in this case is simulated rather than observed) is to a large extent controlled by the overriding synoptic conditions, and that long-term changes in these synoptic conditions are the key drivers of long-term changes in local variables. The series of daily fields of precipitation, temperature and incoming shortwave radiation for the period 2005–2011 are modeled in terms of 11 predictors taken from the NCEP-NCAR reanalysis data at a grid point some 250 km upstream (west) of the NPI, which include atmospheric temperature, relative humidity, zonal moisture flux and meridional moisture flux at different pressure levels (Schaefer et al., 2013). The correlations between the daily averaged output of the WRF-model and the statistical downscaling technique at the different grid point range between 0.65 and 0.80 for precipitation, 0.85–0.93 for temperature and 0.56–0.77 for solar radiation and indicate that the statistical downscaling is applicable.

A further downscaling of the input data of the mass balance model is realized to obtain input data with a resolution of 180 m, the resolution used for the surface mass balance model. Temperature and precipitation are "physically interpolated" by applying constant lapse rates (−0.65 °C/100 m and 5 %/100 m respectively) and incoming solar radiation on the 180 m grid is computed by comparing the radiation computed for the 5 km grid with calculations from clear-sky radiation on the 180 m grid (Schaefer et al., 2013; Corripio, 2003).

In the surface mass balance model ablation was calculated according to a simplified energy balance model (Oerlemans, 2001; Machguth et al., 2009): the net short-wave radiation was determined by the incoming solar radiation and three different albedo values for snow (0.7), firn (0.45) and ice (0.3), whilst the sum of the net long-wave radiation and the turbulent fluxes was approximated by a linear function in temperature. Accumulation at every grid cell was determined as a fraction of total precipitation which varied between zero and one depending on the temperature of the grid cell (Schaefer et al., 2013).

3 Results and discussion

The result of the downscaling process are daily maps of the surface mass balance input variables temperature, incoming solar radiation and precipitation at the resolution of the mass balance model. In Fig. 2a, we present the long-term pattern of incoming solar radiation (averaged over 1975–2011). A sharp north-south cut is visible in the map. West of the cut the yearly average incoming solar energy is below 70 W m^{-2} whilst east of this cut the incoming solar radiation increases, reaching values of up to 150 W m^{-2} on some tongues of the eastern outlet glaciers. On the tongues of north-western outlet glaciers the incoming solar radiation is also increasing up to 100 W m^{-2}. These results of incoming solar radiation reflect well the climatic situation on the SPI where nearly all year long clouds are blocked by the high peaks of the icefields, which reduce the incoming solar radiation. East of the high peaks cloudiness decreases and incoming

solar radiation increases. Several glacier tongues in the north-west of the icefield reach out of this permanent sea of clouds and receive more solar radiation than the center part of the icefield. The downscaled average precipitation map shows a strong increase with elevation due to the generation of orographic precipitation in the regional climate model. East from the Andes main ridge the modeled precipitation decreases rapidly. The temperature decreases with elevation as expected. The results of the downscaling of the meteorological data was compared in detail to meteorological data (Schaefer et al., 2013). Subsequently a calibration of the surface mass balance model has been realized using mass balance measurements in the NPI. Since the climatological situation on the SPI is very similar to the NPI we use the same calibration for the SPI and present surface mass balance simulations for the set of model parameters that performed best on the NPI (Schaefer et al., 2013).

In Fig. 2b we present the distributed annual surface mass balance averaged over 1975–2011. Very positive mass balance of up to 20 mweq is obtained for the very high peaks of the icefield. On the flat plateau the mass balance is between 0 and 5 mweq and on the outlet glacier tongues it reaches down to −15 mweq. The direct (point) observations of the surface mass balance on the SPI are restricted to a network of ablation stakes with changing configuration on the Perito Moreno Glacier during 1995 and 2003 (Stuefer et al., 2007), a tower installed near the equilibrium line of Glacier Chico where yearly mass balance values at one point were obtained from 1994 to 2002 (Rivera, 2004) and four firn cores in the accumulation areas of the Glaciers Moreno (Aristarain and Delmas, 1993), Tyndall (Shiraiwa et al., 2002), Chico (Schwikowski et al., 2006) and PioXI (Schwikowski et al., 2013). In Fig. 3 we compare the results of our simulations to these direct measurements of mass balance. The values in the accumulation area are yearly accumulation values, whilst the ablation data are summer, winter or yearly values depending on the availability of data. The uncertainties of the measurements are indicated as error bars in the x direction if available.

Satisfactory agreement can be observed between the modeled and the measured data. In the accumulation area, in two cases the modeled accumulation is much higher

than the observed one. These two point corresponds to firn cores taken on high peaks in the accumulation areas of the Glaciers Perito Moreno and PioXI. The probably large amounts of snow falling at this locations do not persist on the wind-exposed peaks (Schwikowski et al., 2013). Indeed, some ice core drilling sites were specifically chosen to minimize accumulation compared to the surroundings, to obtain longer time series in the shallow ice cores (Schwikowski et al., 2006). The process of wind drift, however, is not incorporated in the model, which likely explains the difference between observed and modeled value. These local effects are important when comparing point measurements with modeled mass balance, but should not play an important role when estimating the surface mass balance of larger areas as glacier basins or even the entire SPI, since the drifted snow will most probably contribute to the accumulation in another part of the icefield.

The evolution of the annual accumulation, surface ablation and surface mass balance from 1975 to 2010 for the SPI as a whole are presented in Fig. 4.

A high inter-annual variability and an increasing overall trend (0.054 ± 0.012 mweq year^{-1}) of the surface mass balance can be observed. Both the variability and the increasing trend is determined by the accumulation. Furthermore, maxima in accumulation (e.g. 1990, 1998, 2009) are accompanied by minima in ablation, due to albedo feedback mechanisms. The variation of measured yearly precipitation at the selected stations in Fig. 4, is similar to the variation of the modeled accumulation. This is a good confirmation of the model's results, considering that measured precipitation data are no direct input data of the model. The average specific melt on the SPI in 1975–2011 is 2.63 mweq year^{-1} and the average specific accumulation 4.87 mweq year^{-1}. The percentage of solid precipitation of the overall precipitation was 59 %, which leads to an average of 8.36 m of yearly precipitation over the SPI for 1975–2011. This value is 19 % higher than the 7 m inferred by Escobar et al. (1992), analyzing water discharge data from the 1960s to the 1980s. The higher average precipitation over the SPI obtained by our model can be explained by the increase of accumulation (caused by an increase of precipitation) observed in the 2000s. The average modeled

precipitation over SPI is slightly higher than the value of 8.03 m modeled for the NPI (Schaefer et al., 2013). It is expected that the total amount of precipitation over the SPI is higher than on the NPI, since wind speeds, which correlate strongly with precipitation in this region, increase to the south (Garreaud et al., 2012; Lenaerts et al., 2014).

When analyzing another important component of the mass balance of the SPI, namely mass losses due to calving, we will transform the modeled mass losses to losses in volume of ice. We can easily convert the modeled specific mass changes due to surface processes to changes of volume in ice ΔV_{surf} by multiplying with the surface area of the SPI and dividing by the density of ice (900 kg m^{-3}). Knowing the total volume change ΔV_{total} of the SPI from geodetic mass balance surveys (Rignot et al., 2003; Willis et al., 2012b), we can calculate the calving losses from the SPI according to:

$$Q_{\text{c}} = \Delta V_{\text{surf}} - \Delta V_{\text{total}}. \quad (1)$$

In 1975–2000 we obtain an increase of ice volume due to surface processes of 27.7 km^3 year^{-1}. Together with the observed volume loss of 16.7 ± 0.9 km^3 year^{-1} observed for this period by Rignot et al. (2003), we obtain calving losses of $Q_{\text{c}} = 44.4 \pm 0.9$ km^3 year^{-1}. For 2000–2011 we obtain from the observed volume loss of 21.2 ± 0.4 km^3 year^{-1} (Willis et al., 2012b) and the modeled increase in volume due to surface processes of 40.1 km^3 year^{-1} calving losses of $Q_{\text{c}} = 61.3 \pm 0.4$ km^3 year^{-1}. That is, we observe a strong increase in calving losses, which is motivated by an acceleration of the glaciers of SPI (Jaber et al., 2012; Rivera et al., 2012a; Sakakibara et al., 2013). Both authors of the geodetic balances assume that all volume change is due to ice loss and therefore convert volume loss to mass loss assuming a density of 900 kg m^{-3}. Willis et al. (2012b) details volume loss for ablation area and accumulation separately. If we assume that the volume loss in the accumulation area is due melt of firn with a density of 550 kg m^{-3}, the corresponding ice loss would be lower and the calving fluxes would lower to $Q_{\text{c}} = 56.8 \pm 0.2$ km^3 year^{-1}. For comparison, the modeled yearly accumulation over the SPI for 1975–2000 corresponds to 66.7 km^3 of

ice per year and 73.1 km^3 of ice per year for 2000–2011. The modeled melt from SPI is 39.0 km^3 $year^{-1}$ for 1975–2000 and 33.0 km^3 $year^{-1}$ for 2000–2011. Here we used the SPI reference area of 13 000 km^2 from Rignot et al. (2003) to convert the specific values to overall change for 1975–2000 and the area of 12 100 km^2 (Willis et al., 2012b) for 2000–2011.

Apart from the overall trend in the surface mass balance of the SPI it is interesting to analyze the individual glacier catchments as closed systems, to be able to quantify the different contributions of the terms of the mass balance for the different glaciers. However, due to the large flat areas on the SPI, the definition of the catchments (especially in the northern part of the SPI) is not unique and probably also changing through time (Rivera et al., 2012a). In Fig 2c we present the 1975–2011 average specific annual surface mass balance of the individual glaciers using the catchments defined in the Randolph Glacier Inventory (RGI) (Arendt, 2012). In the northern part of the SPI (north of 49.5° S) the main glaciers have annual glacier surface mass balances ranging form slightly negative (Chico Glacier −1.58 mweq) to clearly positive (PioXI Glacier 3.45 mweq). The only exception is Occidental Glacier having a clearly negative annual surface mass balance (−4.85 mweq). Since this glacier does not show an exceptional retreat or thinning behavior (López et al., 2010; Willis et al., 2012b), we think that the exceptionally negative glacier surface mass balance is caused by an erroneous delineation of glacier catchments where parts of the glacier's accumulation area were considered as belonging to neighboring glaciers. The Glacier PioXI has the most positive annual surface mass balance in the area, which agrees with the advance of the glacier observed until recently (Rivera et al., 1997).

In the middle-southern part of the SPI (between 49.5° S and 50.5° S), the annual surface mass balance of the western glaciers are very positive (up to 10.0 mweq for Glacier HPS13) and moderately positive for the eastern glaciers. The very positive modeled surface mass balance of the western glaciers agrees with the accumulation area ratios of > 0.8 observed at these glaciers (Aniya et al., 1996; Casassa et al., 2013).

Apart from mass loss due to surface melt, nearly all major outlet glaciers of the SPI have additional mass losses due to calving (Warren and Aniya, 1999), which makes the total mass balance of the glaciers negative. Calving fluxes Q_c can be inferred for the individual catchments using Eq. (1) again. In Table 1 we present the inferred calving fluxes in 1975–2000 and 2000–2011 for the most important outlet glaciers of the SPI. Since the ice divides in the flat parts of the SPI are difficult to determine, in Table 1 we present the Glaciers Bernardo, Greve, Occidental and Tempano in the north of the SPI as one glacier (BGOT) as well as the glaciers Chico and Viedma (CV) which share the glacier plain around the Paso de los Cuatro Glaciares. The uncertainties of the inferred calving fluxes presented in Table 1 are the uncertainties of the geodetic measurements. For calving fluxes from 2000–2011 we present a range, which is obtained by converting the volume loss in the accumulation area detected by Willis et al. (2012b) to mass loss using the density of firn (550 kg m^{-3}) as lower limit and the density of ice (900 kg m^{-3}) as upper limit.

To validate the inferred calving fluxes, we computed calving fluxes from a complete velocity field of the SPI obtained from a speckle-tracking analysis of RADARSAT-1 images from September 2004 to November 2004. For every glacier we computed the average velocity at the front $\overline{V}$ and derived calving flux from the width at the front W, $\overline{V}$ and the average ice thickness at the front $\overline{H}$. The latter, however, was mostly unknown. Bathymetric measurements of the water bodies in which the glaciers are calving were available for the glaciers Jorge Montt (Rivera et al., 2012b), O'Higgins (unpublished data), Perito Moreno (Rott et al., 1998), Upsala (Skvarca et al., 2003), PioXI (Warren and Rivera, 1994) and Tyndall (Raymond et al., 2005), which provided a good constraint to the ice thickness at the front. There exist bathymetric measurements from Chilean Navy Hydrographic and Oceanographic Service (SHOA) in many Patagonian fjords as well, but mostly they are not extending towards the glacier fronts. In Fig. 1 we present some point measurements from SHOA. So, for most of the other glaciers, an ice thickness of 300 ± 250 m was assumed, which means that we assign a 68 % probability to the event that at an arbitrary calving glacier tongue of the SPI has an

ice thickness between 50 and 550 m. This is motivated by our experience that calving glaciers of similar size have normally ice cliffs of 50 m and larger and are normally not able to persist in water bodies of depth greater than 500 m. For Chico Glacier we estimated $\overline{H} = 100 \pm 50$ m. Calving fluxes were computed according to $Q_c = \overline{V} \cdot \overline{H} \cdot W$, where the products were obtained for every tongue and summed up in the case of several tongues (BGOT for example). The obtained calving fluxes, together with the explicit data for mean velocity, tongue width and estimated ice thickness are presented in Table 1 as well. The uncertainties of the calving fluxes estimated from the velocity field are dominated by the uncertainties of the ice thickness.

The comparison of the inferred calving fluxes with the calving fluxes computed from the velocity field in spring 2004 shows that the inferred calving fluxes are systematically higher. One immediate explanation for this is that at the glacier fronts the method of speckle-tracking analysis of RADARSAT-1 images does not work very well due to loss of coherence caused by high melt rates, fast ice deformation and change of patterns (Warren and Aniya, 1999) and therefore the data presented in Table 1 do not always correspond to the glacier's velocity right at the glacier front. Since calving glaciers normally show high shear rates at the glacier fronts (for example San Rafael Glacier, Willis et al., 2012a), this leads to an underestimation of the calving flux. This might explain the discrepancy between inferred calving fluxes and the calving fluxes estimated from the velocity measurements for the glaciers Europa, HPS12, HPS12, HPS19, HPS31, Penguin and PioXI. An explanation for the higher inferred calving fluxes in 2000–2011 could also be that glacier accelerated since spring 2004.

For the glaciers Moreno, Grey and Tyndall, however, the velocity data from the speckle-tracking analysis of RADARSAT-1 images are available at the front of the glaciers. And for Glacier Perito Moreno similar velocity data were obtained before and after 2004 (Rott et al., 1998; Ciappa et al., 2010). Therefore we think that for these three glaciers the inferred calving fluxes overestimates the real calving fluxes. According to Eq. (1), this disagreement could be due to an overestimation of the modeled

surface mass balance or an overestimation of the volume losses by the geodetic mass balances. Or due to another process of mass change which is not considered in Eq. (1).

Since there are four active volcanoes that coincide with the Southern part of the SPI (see Fig. 1), volcanic activity could induce sub-glacial melt which would lower the mass balance of the glaciers and possibly explain the discrepancy between inferred calving fluxes and measured ones. However, assuming a high constant geothermal heat flow of 1000 mW m^{-2} (mean heat flow over the continental crust is 65 mW m^{-2}), would only lower the specific mass balance by 0.09 mweq. On a glacier like Perito Moreno for example this would only cause an additional mass loss of 0.03 km^3, a very low value compared to the high mass turn-over of the glacier and the large uncertainties concerning the calving fluxes.

Since the modeled ablation at Perito Moreno Glacier agreed well with the observations (Fig. 3), we think that the overestimation of the mass balance might stem from a local overestimation of the accumulation. Since the thinning observed in the geodetic mass balances (Rignot et al., 2003; Willis et al., 2012b) at Glacier Perito Moreno contradicts its stable behavior with even some advances observed during the end of the 20th century and the beginning of the 21st century, we also can not exclude an overestimation of the mass loss by the geodetic balances.

Not very coherent data on calving fluxes could be inferred for the CV glacier complex. Whilst in 1975–2000 the modeled surface mass balance is more negative than the observed losses (which produces the negative calving fluxes), the high thinning observed in 2000–2011 seem to disagree with the moderate calving estimated from the velocity data. Here, we think that different definition of the glacier catchments at the glacier plain of the Paso de los Cuatro Glacieres and the ice divide between the Glaciers Upsala and Viedma and even a migration of ice divides might be the reason for the inconsistent data obtained from the application of Eq. (1).

4 Conclusions

In this contribution we present a first quantification of mass balance processes for the Southern Patagonia Icefield. We conclude that the surface mass balance of the SPI is positive and that it was increasing during 1975–2011. The increase and the variability of the modeled surface mass balance was determined by the accumulation which was 67.7 km^3 of ice per year on average in 1975–2011. The modeled average surface melt was 36.5 km^3 of ice per year and showed good agreement with sparse data from stakes. Using overall balances from geodetic mass balance surveys, calving fluxes could be inferred from the modeled surface mass balance. The inferred losses due to calving showed a strong increase from 44.4 km^3 (1975–2000) to 61.3 km^3 ice per year (2000–2011). In both cases they were higher than losses due to ice and snow melt (39 km^3 and 33 km^3 of ice per year respectively). However, geodetic mass balance surveys are subject to important uncertainties, because of the often unknown density in the accumulation area of the glaciers. Assuming a density of 550 $kg\,m^{-3}$ (instead of 900 $kg\,m^{-3}$) in the accumulation area of SPI, for example, would lower the inferred calving fluxes in 2000–2011 to 56.8 $km^3\,year^{-1}$.

Comparison of the inferred calving fluxes of the most important outlet glaciers with calving fluxes estimated from a velocity field obtained in spring 2004, showed satisfactory agreement for several glaciers. However, the uncertainties of the calving fluxes estimated from the velocity data are large, due to the mostly unknown ice thickness at the glaciers' fronts. On some glaciers the inferred calving fluxes seem to overestimate the possible losses due to calving. Therefore, the inferred overall calving fluxes should be better interpreted as an upper boundary.

Long-term velocity measurements and ice-thickness measurements at the calving front of the glaciers are necessary to better constrain the calving losses from the SPI. Ablation measurements at more glaciers (especially at the western side of the SPI) could help to better judge the performance of surface mass balance models on the SPI. Since precipitation is one of the most insecure output of regional climate models,

spatially distributed accumulation measurements could help to better judge the performance of these models. Appropriate sites for accumulation measurements are smooth and rather flat areas in the central plateau of the accumulation area of the glaciers at elevations of about 1500 m a.s.l. and not wind exposed peaks and ridges where snow drift is dominating the accumulation patterns.

Acknowledgements. The authors would like to thank the Chilean Weather Service (DMC) and the Chilean Water Directory (DGA) for providing meteorological data, Andres Rivera for sharing the data of his Ph.D.-thesis, Mike Willis for sharing the glacier outlines used in his work and the Chilean Navy Hydrographic and Oceanographic Service (SHOA) for providing bathymetric data for the Patagonian fjords. M. Schaefer is FONDECYT Postdoc Fellow (project number 3140135). This work was partly supported by funding from the ice2sea programme from the European Union 7th Framework Programme, grant number 226375. Ice2sea contribution number 168.

References

Aniya, M., Sato, H., Naruse, R., Skvarca, P., and Casassa, G.: The use of satellite and airborne imagery to inventory outlet glaciers of the Southern Patagonia Icefield, South America, Photogramm. Eng. Rem. S., 62, 1361–1369, 1996. 3125

Aravena, J.-C. and Luckman, B. H.: Spatio-temporal rainfall patterns in southern South America, Int. J. Climatol., 29, 2106–2120, doi:10.1002/joc.1761, 2009. 3119

Arendt, E. A.: Randolph Glacier Inventory [v3.0]: A Dataset of Global Glacier Outlines, Tech. rep., Global Land Ice Measurements from Space, Boulder, Colorado, USA, 2012. 3125

Aristarain, A. and Delmas, R.: Firn-core study from the Southern Patagonia Ice Cap, South America, J. Glaciol., 39, 249–254, 1993. 3122

Carrasco, J., Casassa, G., and Rivera, A.: Meteorological and climatological aspects of the Southern Patagonia Icefield, in: The Patagonian Icefields – A Unique Natural Laboratory for Environmental and Climate Change Studies, Kluwer Academic/Plenum Publishers, New York, Boston Dordrecht, London, Moscow, 29–41, 2002. 3119

Casassa, G., Rodríguez, J. L., and Loriaux, T.: A New Glacier Inventory for the Southern Patagonia Icefield and Areal Changes 1986–2000, in: Global Land Ice Measurements from Space, Springer Praxis Books, New York, 2013. 3125

Ciappa, A., Pietranera, L., and Battazza, F.: Perito Moreno Glacier (Argentina) flow estimation by COSMO SkyMed sequence of high-resolution SAR-X imagery, Remote Sens. Environ., 114, 2088–2096, 2010. 3127

Corripio, J.: Vectorial algebra algorithms for calculating terrain parameters from DEMs and solar radiation modelling in mountainous terrain, Int. J. Geogr. Inf. Sci., 17, 1–23, doi:10.1080/713811744, 2003. 3121

Escobar, F., Vidal, F., Garin, C., and Naruse, R.: Water balance in the Patagonia Icefield, Tech. rep., Institute of Low Temperature Research, Sapporo, 1992. 3123

Falvey, M. and Garreaud, R. D.: Regional cooling in a warming world: recent temperature trends in the southeast Pacific and along the west coast of subtropical South America (1979–2006), J. Geophys. Res., 114, D04102, doi:10.1029/2008JD010519, 2009. 3119

Fowler, H. J., Blenkinsopa, S., and Tebaldib, C.: Linking climate change modelling to impacts studies: recent advances in downscaling techniques for hydrological modelling, Int. J. Climatol., 27, 1547–1578, 2007. 3120

Garreaud, R. and Lopez, P., Minvielle, M., and Rojas, M.: Large scale control on the Patagonia climate, J. Climate, 26, 215–230, 2012. 3124

Ibarzabal y Donangelo, T., Hoffmann, J., and Naruse, R.: Recent climate changes in southern Patagonia, Bulletin of Glacier Research, 14, 29–36, 1996. 3119

Jaber, W. A., Floricioiu, D., Rott, H., and Eineder, M.: Dynamics of fast glaciers in the Patagonia Icefields derived from Terrasar-X and Tandem-X data, in: Geoscience and Remote Sensing Symposium (IGARSS), 2012 IEEE International, Munich, 22–27 July 2012, 3226–3229, doi:10.1109/IGARSS.2012.6350737, 2012. 3119, 3124

Kalnay, E., Kanamitsu, M., Kistler, R., Collins, W., Deaven, D., Gandin, L., Iredell, M., Saha, S., White, G., Woollen, J., Zhu, Y., Chelliah, M., Ebisuzaki, W., Higgins, W., Janowiak, J., Mo, K., Ropelewski, C., Wang, J., Leetmaa, A., Reynolds, R., Jenne, R., and Joseph, D.: The NCEP/NCAR 40-year reanalysis project, B. Am. Meteorol. Soc., 77, 437–471, doi:10.1175/1520-0477(1996)077<0437:TNYRP>2.0.CO;2, 1996. 3120

Lenaerts, J. T. M., van den Broeke, M. R., van Wessem, J. M., van de Berg, W. J., van Meijgaard, E., van Ulft, L. H, and Schaefer, M.: Extreme precipitation and climate gradients in

Patagonia revealed by high-resolution regional atmospheric climate modelling, J. Climate, 27, 4607–4621, 2014. 3124

López, P., Chevallier, P., Favier, V., Pouyaud, B., Ordenes, F., and Oerlemans, J.: A regional view of fluctuations in glacier length in southern South America, Global Planet. Change, 71, 85–108, 2010. 3118, 3125

Machguth, H., Paul, F., Kotlarski, S., and Hoelzle, M.: Calculating distributed glacier mass balance for the Swiss Alps from regional climate model output: a methodical description and interpretation of the results, J. Geophys. Res.-Atmos., 114, D19106, doi:10.1029/2009JD011775, 2009. 3121

Masiokas, M. H., Rivera, A., Espizua, L. E., Villalba, R., Delgado, S., and Carlos Aravena, J.: Glacier fluctuations in extratropical South America during the past 1000 years, Palaeogeogr. Palaeocl., 281, 242–268, doi:10.1016/j.palaeo.2009.08.006, 2009. 3118

Oerlemans, J.: Glaciers and Climate Change, A. A. Balkema Publishers, Lisse, Abingdon, Exton, Tokyo, 2001. 3119, 3121

Orihashi, Y., Naranjo, J., Motoki, A., Sumino, H., Hirata, D., Anma, R., and Nagao, K.: The Quaternary volcanic activity of Hudson and lautaro volcanoes, Chilean Patagonia: new age constraints from K-Ar ages, Rev. Geol. Chile, 31, 207–224, 2004. 3118

Rasmussen, L. A., Conway, H., and Raymond, C. F.: Influence of upper air conditions on the Patagonia icefields, Global Planet. Change, 59, 203–216, doi:10.1016/j.gloplacha.2006.11.025, 2007. 3119

Raymond, C., Neumann, T., Rignot, E., Echelmeyer, K., Rivera, A., and Casassa, G.: Retreat of Glaciar Tyndall, Patagonia, over the last half-century, J. Glaciol., 51, 239–247, doi:10.3189/172756505781829476, 2005. 3126

Rignot, E., Rivera, A., and Casassa, G.: Contribution of the Patagonia Icefields of South America to sea level rise, Science, 302, 434–437, doi:10.1126/science.1087393, 2003. 3118, 3119, 3124, 3125, 3128, 3135

Rivera, A.: Mass balance investigations at Glaciar Chico, Southern Patagonia Icefield, Chile, Ph.D. thesis, University of Bristol, Bristol, 2004. 3119, 3122

Rivera, A., Lange, H., Aravena, J., and Casassa, G.: The 20th-century advance of Glaciar Pio XI, Chilean Patagonia, Ann. Glaciol., 24, 66–71, 1997. 3125

Rivera, A., Corripio, J., Bravo, C., and Cisternas, S.: Glaciar Jorge Montt (Chilean Patagonia) dynamics derived from photos obtained by fixed camera and satellite image feature tracking, Ann. Glaciol., 53, 147–155, 2012a. 3119, 3124, 3125

Rivera, A., Koppes, M., Bravo, C., and Aravena, J. C.: Little Ice Age advance and retreat of Glaciar Jorge Montt, Chilean Patagonia, Clim. Past, 8, 403–414, doi:10.5194/cp-8-403-2012, 2012b. 3126

Rosenblüth, B., Casassa, G., and Fuenzalida, H.: Recent climatic changes in western Patagonia, Bulletin of Glacier Research, 13, 127–132, 1995. 3119

Rott, H., Stuefer, M., Siegel, A., Skvarca, P., and Eckstaller, A.: Mass fluxes and dynamics of Moreno Glacier, Southern Patagonia Icefield, Geophys. Res. Lett., 25, 1407–1410, doi:10.1029/98GL00833, 1998. 3126, 3127

Sakakibara, D., Suggiyama, S., Sawagaki, T., Marinsek, S., and Skvarca, P.: Rapid retreat, acceleration and thinning of Glaciar Upsala, Southern Patagonia Icefield, initiated 2008, Ann. Glaciol., 54, 131–138, 2013. 3119, 3124

Schaefer, M., Machguth, H., Falvey, M., and Casassa, G.: Modeling past and future surface mass balance of the Northern Patagonian Icefield, J. Geophys. Res.-Earth, 118, 571–588, doi:10.1002/jgrf.20038, 2013. 3119, 3120, 3121, 3122, 3124

Schwikowski, M., Bruetsch, S., Casassa, G., and Rivera, A.: A potential high-elevation ice-core site at Hielo Patagónico Sur, Ann. Glaciol., 43, 8–13, doi:10.3189/172756406781812014, 2006. 3122, 3123

Schwikowski, M., Schläppi, M., Santibañez, P., Rivera, A., and Casassa, G.: Net accumulation rates derived from ice core stable isotope records of Pío XI glacier, Southern Patagonia Icefield, The Cryosphere, 7, 1635–1644, doi:10.5194/tc-7-1635-2013, 2013. 3122, 3123

Shiraiwa, T., Kohshima, S., Uemura, R., Yoshida, N., Matoba, S., Uetake, J., and Godoi, M.: High net accumulation rates at Campo de Hielo Patagonico Sur, South America, revealed by analysis of a 45.97 m long ice core, Ann. Glaciol., 35, 84–90, doi:10.3189/172756402781816942, 2002. 3122

Skvarca, P., Raup, B., and De Angelis, H.: Recent behaviour of Glaciar Upsala, a fast-flowing calving glacier in Lago Argentino, southern Patagonia, Ann. Glaciol., 36, 184–188, doi:10.3189/172756403781816202, 2003. 3126

Stern, C.: Active Andean volcanism: its geologic and tectonic setting, Rev. Geol. Chile, 31, 161–206, 2004. 3118

Stern, C.: Holocene tephrochronology record of large explosive eruptions in the southernmost Patagonian Andes, B. Volcanol., 70, 435–454, 2008. 3118

Stuefer, M., Rott, H., and Skvarca, P.: Glaciar Perito Moreno, Patagonia: climate sensitivities and glacier characteristics preceding the 2003/04 and 2005/06 damming events, J. Glaciol., 53, 3–15, 2007. 3119, 3122

Warren, C. and Aniya, M.: The calving glaciers of southern South America, Global Planet. Change, 22, 59–77, doi:10.1016/S0921-8181(99)00026-0, 1999. 3126, 3127

Warren, C. and Rivera, A.: Non-linear climatic response of Calving Glaciers: a case study of Pio XI Glacier, Chilean Patagonia, Rev. Chil. Hist. Nat., 67, 385–394, 1994. 3126

Willis, M. J., Melkonian, K., Pritchard, M., and Ramage, J.: Ice loss rates at the Northern Patagonian Icefield derived using a decade of satellite remote sensing, Remote Sens. Environ., 117, 184–198, 2012a. 3119, 3127, 3135

Willis, M. J., Melkonian, K., Pritchard, M., and Rivera, A.: Ice loss from the Southern Patagonian Ice Field, South America, between 2000 and 2012, Geophys. Res. Lett., 39, L17501, doi:10.1029/2012GL053136 2012b. 3118, 3124, 3125, 3126, 3128

Table 1. Inferred calving fluxes according to Eq. (1) using the geodetic mass balance measurements of Rignot et al. (2003) for the period 1975–2000 and of Willis et al. (2012a) for 2000–2011 (first two columns). Calving fluxes based on a velocity-map from spring 2004 (third column) and explicit data used to compute these fluxes (columns four to six). Column seven indicates if the calving fluxes computed from the velocity field agree with the inferred fluxes for 1975–2000 (R) or 2000–2011 (W) or both (RW).

Glacier	Q_c Inferred 1975–2000 (km^3)	Q_c Inferred 2000–2011 (km^3)	Q_c From velocities Spring 2004 (km^3)	W_{tot} (km)	$\overline{V}$ (km year^{-1})	$\overline{H}$ (m)	Agreement within 1σ
Amalia	0.69 ± 0.05	(0.92–0.96) ± 0.07	0.42 ± 0.35	2.45	0.57	300 ± 250	R
Asia	0.38 ± 0.03	(0.48–0.50) ± 0.05	0.26 ± 0.21	0.85	1	300 ± 250	RW
BGOT	0.86 ± 0.18	(1.72–2.12) ± 0.18	1.8 ± 1.03	12.51	0.48	300 ± 250	RW
CV	−1.48 ± 0.24	(1.86–2.25)±0.09	0.36 ± 0.3	1.97	0.41	230 ± 180	–
Europa	no data	(2.75–2.81) ± 0.08	0.41 ± 0.34	0.92	1.48	300 ± 250	–
Grey	1.16 ± 0.05	(1.51–1.55) ± 0.10	0.39 ± 0.32	2.17	0.47	300 ± 250	–
HPS12	no data	(1.38–1.43) ± 0.05	0.55 ± 0.46	0.8	2.29	300 ± 250	–
HPS13	no data	(1.37–1.38) ± 0.04	01.07 ± 0.89	0.94	3.8	300 ± 250	W
HPS15	no data	(0.85–0.88) ± 0.04	0.55 ± 0.46	0.92	2	300 ± 250	W
HPS19	no data	(1.37–1.42) ± 0.06	0.43 ± 0.36	0.75	1.93	300 ± 250	–
HPS29	0.52 ± 0.02	(0.57–0.6) ± 0.05	0.52 ± 0.43	1.22	1.41	300 ± 250	RW
HPS31	0.91 ± 0.03	(1.04–1.08) ± 0.06	0.41 ± 0.34	0.75	1.80	300 ± 250	–
HPS34	1.40 ± 0.03	(1.66–1.72) ± 0.06	0.85 ± 0.71	1.89	1.50	300 ± 250	RW
Jorge Montt	1.03 ± 0.10	(1.43–1.58) ± 0.06	1.20 ± 0.54	2.1	2.59	220 ± 50	RW
O'Higgins	2.40 ± 0.15	(2.97–3.27) ± 0.13	1.78 ± 0.52	2.33	2.25	340 ± 100	R
Penguin	no data	(4.61–4.72) ± 0.08	0.83 ± 0.69	1.2	2.30	300 ± 250	–
Perito Moreno	0.89 ± 0.04	(1.44–1.57) ± 0.08	0.44 ± 0.16	4.9	0.65	140 ± 50	–
Pío XI	3.76 ± 0.32	(5.99–6.35) ± 0.14	2.69 ± 1.71	9.82	1.74	200 ± 100	R
Tyndall	0.80 ± 0.06	(1.58–1.69) ± 0.11	0.14 ± 0.08	2.28	0.35	181 ± 100	–
Upsala	1.83 ± 0.17	(4.67–5.05) ± 0.08	2.41 ± 0.40	2.64	1.52	540 ± 100	R

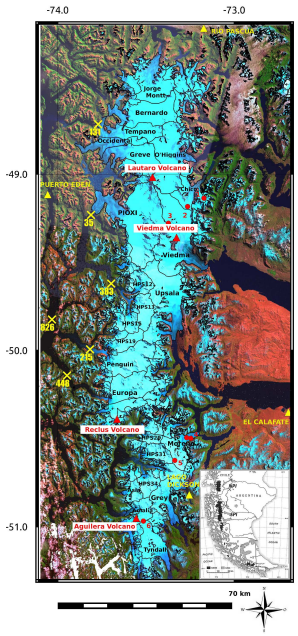

Figure 1. The Southern Patagonia Icefield (SPI): false-colour composite of Landsat ETM+ satellite image mosaic; names of examined glacier catchments in black; yellow triangles mark the positions of some of the meteorological stations that were used to validate the downscaling of the reanalysis data; red dots mark direct mass balance measurements on the SPI (1–6); the four active volcanoes that coincide with the SPI are represented by red triangles. The yellow crosses with numbers mark individual measurements of fjord depth provided by the Chilean Navy Hydrographic and Oceanographic Service (SHOA). Inset: position of the SPI in Southern South America.

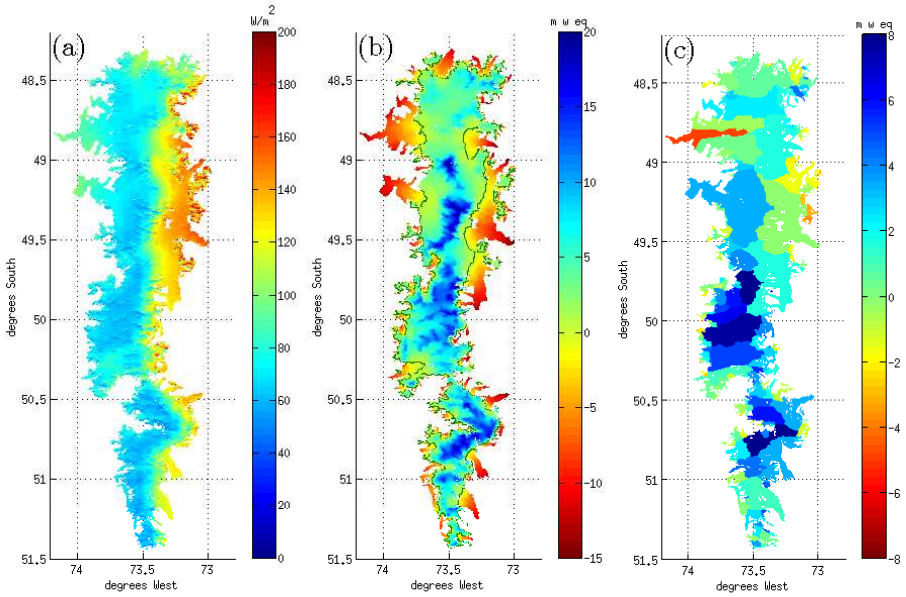

Figure 2. Maps of **(a)** downscaled incoming solar radiation over SPI; **(b)** annual surface mass balance of the SPI (green line denotes zero mass balance); **(c)** annual averaged glacier mass balance. All maps show averages 1975–2011.

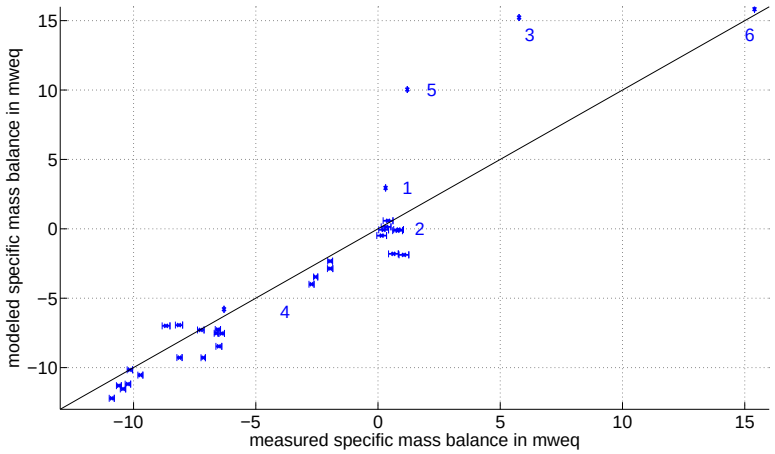

Figure 3. Comparison between measured and simulated mass balance; labels correspond to places marked in Fig. 1.

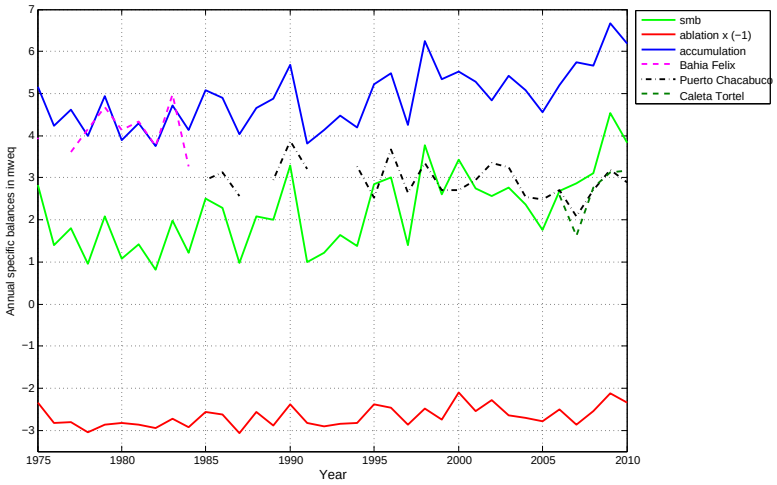

Figure 4. Annual specific accumulation, ablation and surface mass balance (smb) averaged over the SPI from 1975–2010 and yearly measured precipitation sums for selected weather stations in the region: Bahía Felix (52°58′ S, 74°08′ W) south of the SPI, Puerto Chacabuco (45°26′ S, 72°49′ W) north of the NPI and Caleta Tortel (47°47′ S, 73°32′ W) between NPI and SPI.